

Machine Learning-Assisted Fabrication of PCBM-Perovskite Solar Cells with Nanopatterned TiO₂ Layer

Siti Norhasanah Sanimu¹, Hwa-Young Yang², Jeevan Kandel¹, Ye-Chong Moon¹, Gangasagar Sharma Gaudel¹, Seung-Ju Yu¹, Yong Ju Kim¹, Sejung Kim¹, Bong-Hyun Jun³, and Won-Yeop Rho¹

¹Jeonbuk National University

²Ulsan National Institute of Science and Technology

³Konkuk University

April 30, 2023

Abstract

To unlock the full potential of PSCs, machine learning (ML) was implemented in this research to predict the best combination of mesoporous-titanium dioxide (mp-TiO₂) and weight percentage (wt%) of phenyl-C₆₁-butyric acid methyl ester (PCBM), along with the current density (J_{sc}), open-circuit voltage (V_{oc}), fill factor (ff) and energy conversion efficiency (ECE). Then, the combination that yielded the highest predicted ECE was selected as a reference to fabricate PCBM-PSCs with nanopatterned TiO₂ layer. Subsequently, the PCBM-PSCs with nanopatterned TiO₂ layers were fabricated and characterized to further understand the dual effects of nanopatterning depth and wt% of PCBM on PSCs. Experimentally, the highest ECE of 17.336% is achieved at 127 nm nanopatterning depth and 0.10 wt% of PCBM, where the J_{sc} , V_{oc} and ff are 22.877 mA/cm², 0.963 V and 0.787, respectively. The measured J_{sc} , V_{oc} , ff and ECE values show consistencies with the ML prediction. Hence, these findings not only revealed the potential of ML to be used as a preliminary investigation to navigate the research of PSCs, but also highlighted that nanopatterning depth has a significant impact on J_{sc} , and the incorporation of PCBM on perovskite layer influenced the V_{oc} and ff , which further boosted the performance of PSCs.

Article category: Research Article

Subcategory: Perovskite Solar Cell

Machine Learning-Assisted Fabrication of PCBM-Perovskite Solar Cells with Nanopatterned TiO₂ Layer

Hasanah Sanimu⁺, Hwa-Young Yang⁺, Jeevan Kandel⁺, Ye-Chong Moon⁺, Gangasagar Sharma Gaudel⁺, Seung-Ju Yu, Yong Ju Kim^{3*}, Sejung Kim^{*}, Bong-Hyun Jun^{*}, Won-Yeop Rho^{*}

Hasanah Sanimu, Jeevan Kandel, Ye-Chong Moon, Gangasagar Sharma Gaudel, Seung-Ju Yu

Graduate School of Integrated Energy-AI, Jeonbuk National University, 567 Baekje-daero, Deokjin-gu, Jeonju-si, Jeollabuk-do 54896, Republic of Korea

Dr. Hwa-Young Yang

School of Energy and Chemical Engineering, Ulsan National Institute of Science and Technology (UNIST), 50 UNIST-gil, Eonyang-eup, Ulju-gun, Ulsan 44919, Republic of Korea

Prof. Yong Ju Kim

Department of Oriental Medicine Resources, College of Environmental and Bioresource Sciences, Jeonbuk National University, Iksan 54596, Republic of Korea

Email: nationface@jbnu.ac.kr

Prof. Sejung Kim

School of Chemical Engineering, Jeonbuk National University, 567 Baekje-daero, Deokjin-gu, Jeonju-si, Jeollabuk-do 54896, Republic of Korea

Email: sejung.kim@jbnu.ac.kr

Prof. Bong-Hyun Jun

Department of Bioscience and Biotechnology, Konkuk University, 120 Neungdong-ro, Gwangjin-gu, Seoul 05029, Republic of Korea

Email: bjun@konkuk.ac.kr

Prof. Won-Yeop Rho

School of International Engineering and Science, Jeonbuk National University, 567 Baekje-daero, Deokjin-gu, Jeonju-si, Jeollabuk-do 54896, Republic of Korea

Graduate School of Integrated Energy-AI, Jeonbuk National University, 567 Baekje-daero, Deokjin-gu, Jeonju-si, Jeollabuk-do 54896, Republic of Korea

Email: rho7272@jbnu.ac.kr

Keywords: perovskite solar cells, nanopatterning, PCBM, machine learning, prediction

Abstract

To unlock the full potential of PSCs, machine learning (ML) was implemented in this research to predict the best combination of mesoporous-titanium dioxide (mp-TiO₂) and weight percentage (wt%) of phenyl-C₆₁-butyric acid methyl ester (PCBM), along with the current density (J_{sc}), open-circuit voltage (V_{oc}), fill factor (ff) and energy conversion efficiency (ECE). Then, the combination that yielded the highest predicted ECE was selected as a reference to fabricate PCBM-PSCs with nanopatterned TiO₂ layer. Subsequently, the PCBM-PSCs with nanopatterned TiO₂ layers were fabricated and characterized to further understand the dual effects of nanopatterning depth and wt% of PCBM on PSCs. Experimentally, the highest ECE of 17.336% is achieved at 127 nm nanopatterning depth and 0.10 wt% of PCBM, where the J_{sc} , V_{oc} and ff are 22.877 mA/cm², 0.963 V and 0.787, respectively. The measured J_{sc} , V_{oc} , ff and ECE values show consistencies with the ML prediction. Hence, these findings not only revealed the potential of ML to be used as a preliminary investigation to navigate the research of PSCs, but also highlighted that nanopatterning depth has a significant impact on J_{sc} , and the incorporation of PCBM on perovskite layer influenced the V_{oc} and ff , which further boosted the performance of PSCs.

1. Introduction

Machine learning (ML), which belongs to an important branch of artificial intelligence, has gained fame in the fields of energy materials and solar cells.^[1] ML is a science of getting computers to perform tasks without being explicitly programmed, and it can learn from past results and provide fast predictions of unknown results.^[2] Furthermore, ML also can infer the potential rules and relationships among materials, and between materials and the features of the complex system composed of materials only through the data itself without knowing the physical laws.^[3] With the proven capabilities of ML, ML can have a significant impact to greatly increase the speed of doing research in perovskite solar cells (PSCs). To optimize PSCs, the conventional method mostly depends on trial-and-error methods, which is not only time consuming, but has limited test options and leads to the cost of opportunity loss by doing something else with the available time. Therefore, by applying ML, researchers may examine a tremendous amount of data on PSCs and make predictions by

uncovering patterns and relationships in the data. These predictions can then be used to guide experiments, enabling researchers to optimize the development of PSCs more efficiently than traditional methods.

Studies have shown that the performance of PSCs is hindered by low light harvesting. Specifically, the ability of PSCs to absorb light drops significantly between 650-800 nm and diminishes further when the wavelength exceeds 800 nm.^[4-6] To overcome this issue, one of the strategies that has been implemented is light scattering. The basic idea of light scattering is to confine light propagation and extend the traveling distance of incident light within the photoelectrode film,^[7] which can be explained using Rayleigh and Mie scattering theories. In general, Rayleigh scattering theory is applicable for small-sized particles, whose diameter is less than about one-tenth the wavelength of the incident light while Mie scattering theory is applicable to large particles, whose diameter is larger than the wavelength of the incident light.^[8] Apart from that, the introduction of nano/microstructures at the glass/air interface have also been reported to increase the incident photon and the generation of photocurrent.^[9, 10] Studies also reported that constructing nano/microstructures at the fluorine-doped tin oxide (FTO)/ titanium dioxide (TiO₂) interface can increase the absorption length for the incident light due to the diffraction effect.^[11-13] Therefore, to increase the light harvesting property in PSCs, Hwa-Young Yang et al. have also shown the relationship between the transmittance and the electron generation by varying the nanopatterning depth of the mesoporous titanium dioxide (mp-TiO₂) layer.^[14]

Next, to improve the electron transport in PSCs, a plethora of materials have been studied and carbon nanomaterials have been widely utilized in PSCs to enhance both the efficiency and stability due to their outstanding chemical, electrical, and mechanical characteristics. It has not only been used as an additive, but has also acted on potential structure alternatives for the charge carrier transportation layer, electrode, and active film.^[15] Among carbon nanomaterials, fullerene nanometric-sized spherical shapes play an important role for efficient interfacing with perovskites, resulting in a homogeneous distribution of the carbon nanomaterials on the surface of light absorber, thus generating highly selective contacts for electron extraction.^[16] Phenyl-C₆₁-butyric acid methyl ester (PCBM), which is a fullerene derivative of the C₆₀, is among the most employed carbon nanomaterials in PSCs due to the alignment of energy levels and high electron mobility.^[17, 18] Previous research has demonstrated that by controlling the amount of PCBM in the lead(II) iodide (PbI₂) precursor solution, the fill factor (ff) increased significantly as PCBM are able to fill in the pinholes and vacancies between perovskite grains that produce continuous pathways for electron extraction. Moreover, when PCBM was mixed with perovskite to create a PCBM-perovskite structure, the charge recombination lifetime and carrier diffusion length increases as the electron was transported over longer distances in the film compared to pure perovskite film.^[19]

Based on the mentioned articles, studies have shown that the most optimized nanopatterning depth will affect the current density (J_{sc}), and the incorporation of PCBM into perovskite is able to significantly enhance the ff of the PSCs. Therefore, with the potential of ML to be used as a preliminary approach, it is expected that the combination of ML with light management and electron transport strategies will yield a better performance of PSCs. Herein, ML is used to assist the fabrication of PCBM-PSCs with nanopatterned TiO₂ layer by deciphering the relationship between nanopatterning depth of mp-TiO₂ and weight percentage (wt%) of PCBM to predict the best combination of the two variables. Not only that, the photovoltaics parameters, that are J_{sc} , open-circuit voltage (V_{oc}), ff and energy conversion efficiency (ECE) are also predicted by the ML. Subsequently, the PCBM-PSCs with nanopatterned TiO₂ layer are prepared and characterized to further understand the dual effects of nanopatterning depth and wt% of PCBM on PSCs. Hence, these findings not only revealed the potential of ML to be used as a preliminary investigation to navigate the research of PSCs, but also highlighted that nanopatterning depths have significant impact on J_{sc} , and the incorporation of PCBM on perovskite layer influenced the V_{oc} and ff , which further boosted the performance of PSCs.

2. Results and Discussion

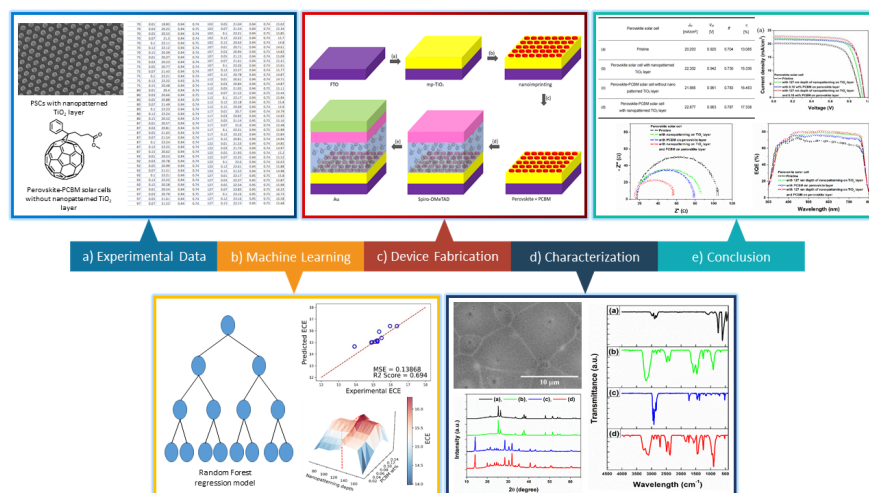


Figure 1 . The overall scheme of using ML to assist the fabrication of PCBM-PSCs with nanopatterned TiO_2 layer, where the process includes a) a collection of experimental data for PSCs with nanopatterned TiO_2 layer and PCBM-PSCs, (b) predictions of J_{sc} , V_{oc} , ff and ECE for the PCBM-PSCs with nanopatterned TiO_2 layer through machine learning, (c) the fabrication of PCBM-PSCs with nanopatterned TiO_2 layer, (d) device characterization and (e) the conclusion for the results obtained.

Figure 1 shows the overall scheme of using ML to assist the fabrication of PCBM-PSCs with nanopatterned TiO_2 layer. The present process involves the collection of experimental data with the J_{sc} , V_{oc} , ff and ECE values for PSCs with nanopatterned TiO_2 layer and PCBM-PSCs as listed in **Table S1** and **Table S2** in the supporting information. The nanopatterning depth of PSCs with nanopatterned TiO_2 layer were varied to 70, 75, 80, 87, 92, 97, 102, 107, 112, 117, 122, 127, 132, 137, 142, 147, 152, 157 and 167 nm while the wt% of PCBM for PCBM-PSCs were varied to 0.01, 0.03, 0.05, 0.07, 0.10, 0.12 and 0.15 wt%. Subsequently, the dataset was used to predict the best combination of nanopatterning depth and the wt% of PCBM, as well as the J_{sc} , V_{oc} , ff and ECE of the PCBM-PSCs with nanopatterned TiO_2 layers. To achieve that goal, a Random Forest (RF) regression model, which is an ensemble method that uses multiple decision trees to improve the prediction accuracy and prevent overfitting was used.^[20] Then, the best combination of nanopatterning depth and wt% of PCBM that yielded the highest ECE was selected as a reference to fabricate the PCBM-PSCs with nanopatterned TiO_2 layer. After the fabrication process, the device was characterized to further understand the dual effects of nanopatterning depth and wt% of PCBM on PSCs. Lastly, the conclusions were deduced based on the results obtained throughout the process.

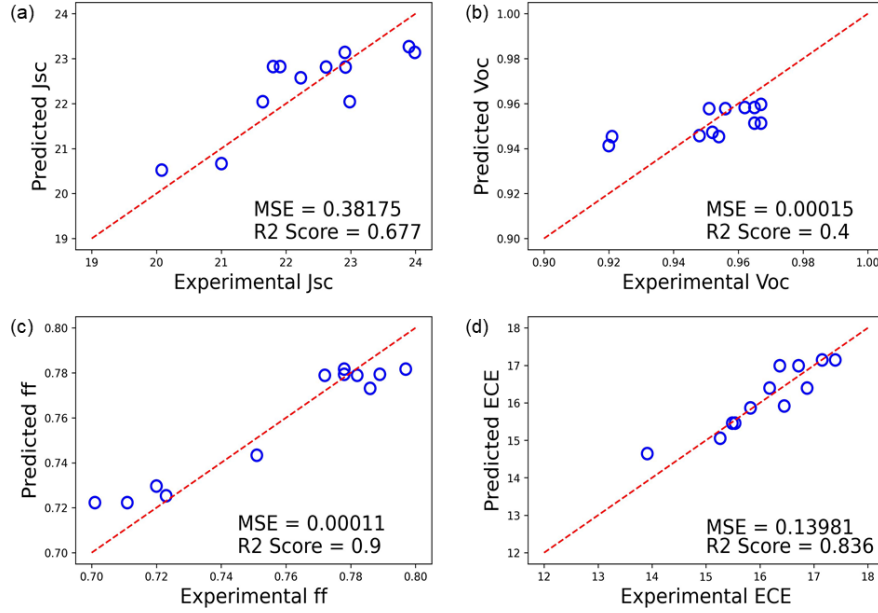


Figure 2 . The performance of Random Forest regression models to predict the a) J_{sc} , b) V_{oc} , c) ff and d) ECE.

As demonstrated in **Figure 2** , the RF regression models were utilized to predict the performance metrics of photovoltaic parameters, including the J_{sc} , V_{oc} , ff and ECE. The performance of the RF model was evaluated by using the coefficient of determination (R^2) and mean squared error (MSE). The R^2 values provide information on how much of the variance is due to the independent variables^[21] while MSE is used to evaluate the quality of fit in terms of distance of the regressor to the actual training points.^[22] The bound for R^2 value is $(-1, 1]$, where -1 indicates the worst output value and 1 indicates the best value. In other words, an output value of R^2 close to 1 suggested a good prediction of the regression model. For MSE, the value is bounded between $[0, +\infty)$ and 0 MSE value is obtained if the linear regression model fits the data perfectly.^[23]

In these predictions, the R^2 values obtained for J_{sc} , V_{oc} , ff and ECE were 0.693, 0.523, 0.839 and 0.694, respectively, and showed that the RF model can explain 69.3%, 52.3%, 83.9% and 69.4% of the variation in the J_{sc} , V_{oc} , ff and ECE with the input features (nanopatterning depth of mp-TiO₂ layer and wt% of PCBM). High R^2 values for J_{sc} , ff and ECE indicate that the RF model effectively captures the relationship between the input features with J_{sc} , ff and ECE, showing the ability of the model to predict accurately. Although the R^2 value for the V_{oc} prediction is the lowest among the four parameters, it does not necessarily indicate that the RF model is less accurate for predicting the V_{oc} , but rather highlights the complex interplay between different factors that influence the performance of the photovoltaic parameters. Despite this, the MSEs for all four parameters were relatively low, suggesting the model can still provide reliable predictions.

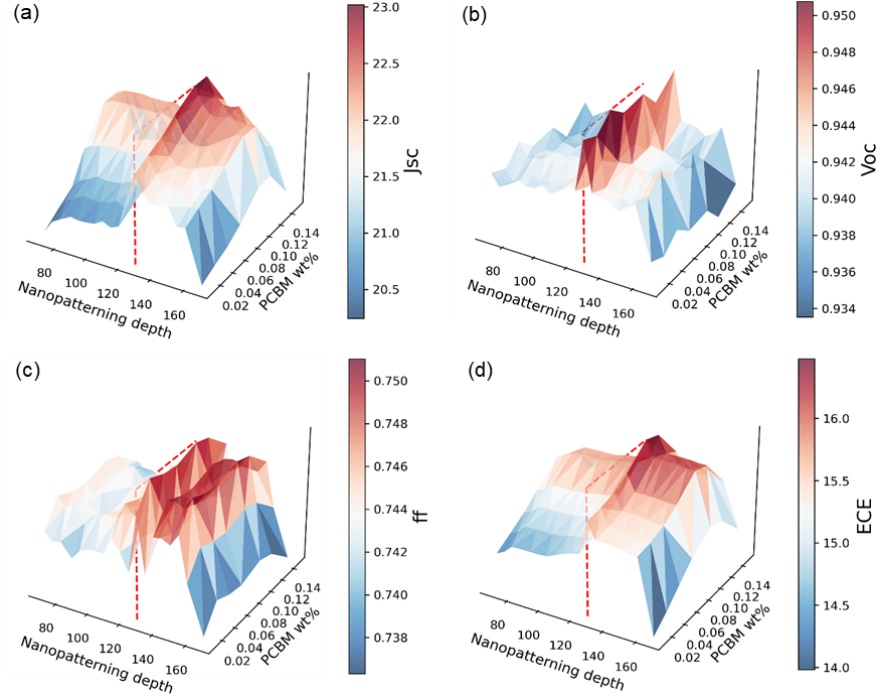
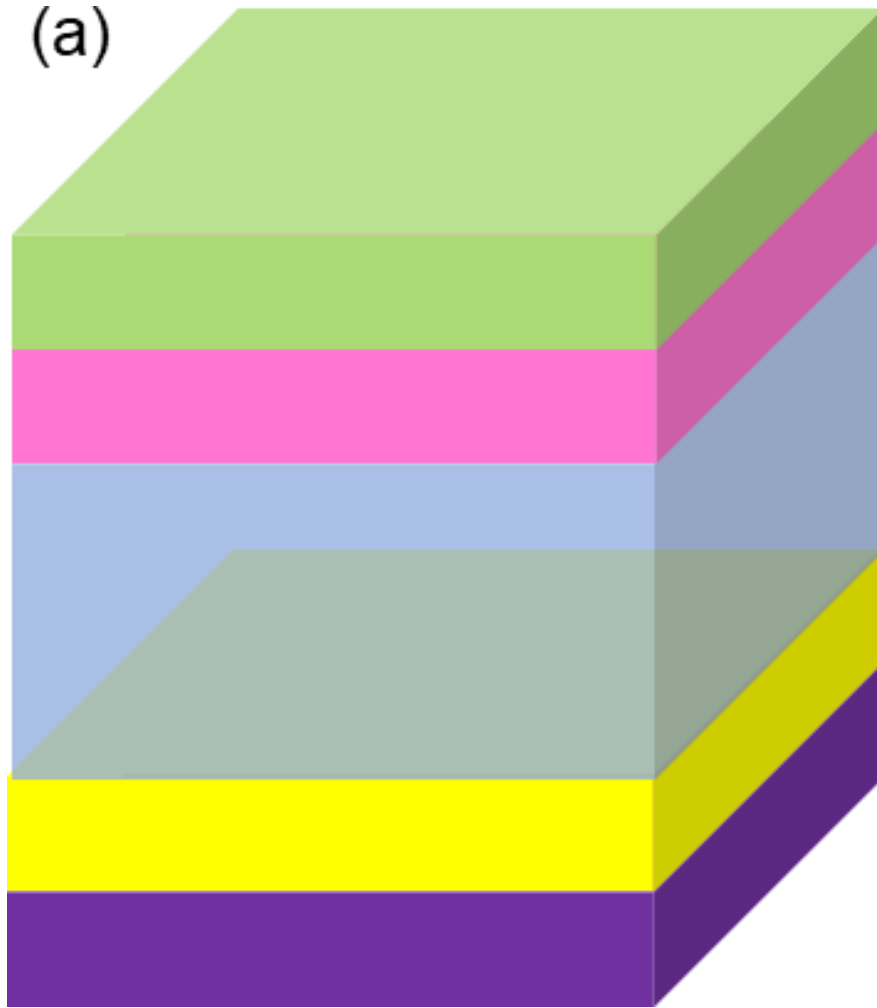


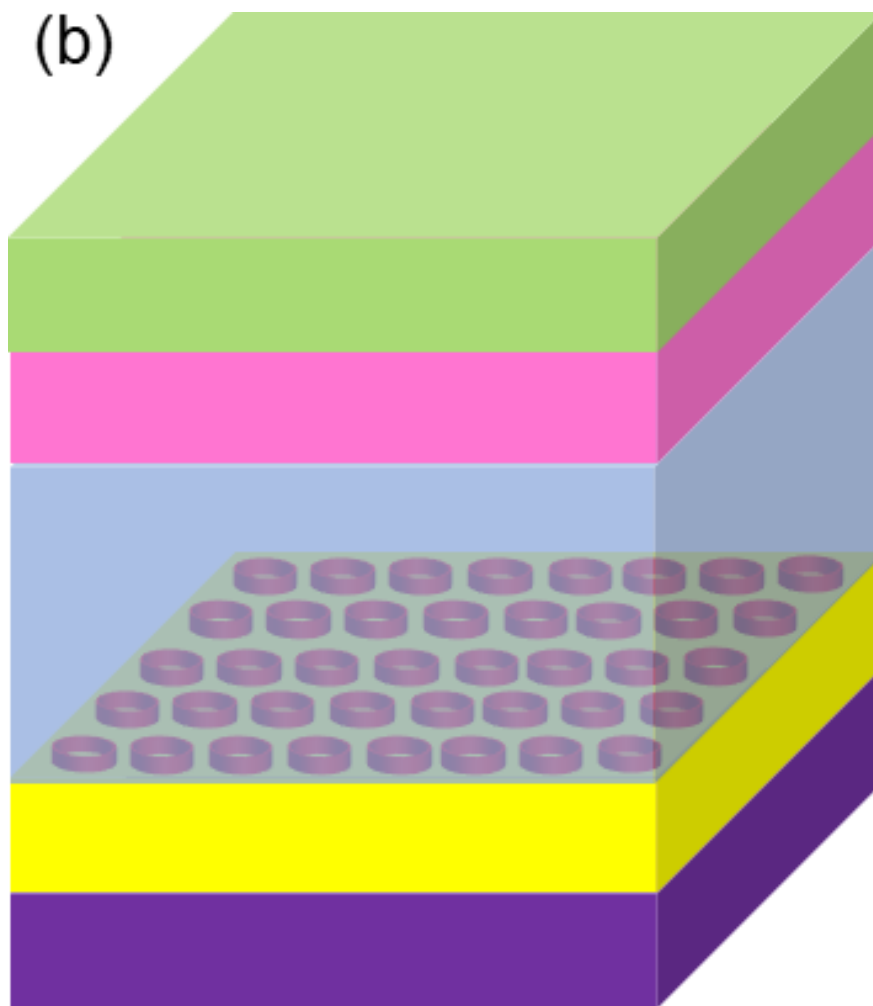
Figure 3 . Predictions of (a) J_{sc} , (b) V_{oc} , (c) ff and (d) ECE of PCBM-PSCs with nanopatterned TiO_2 layers by using ML.

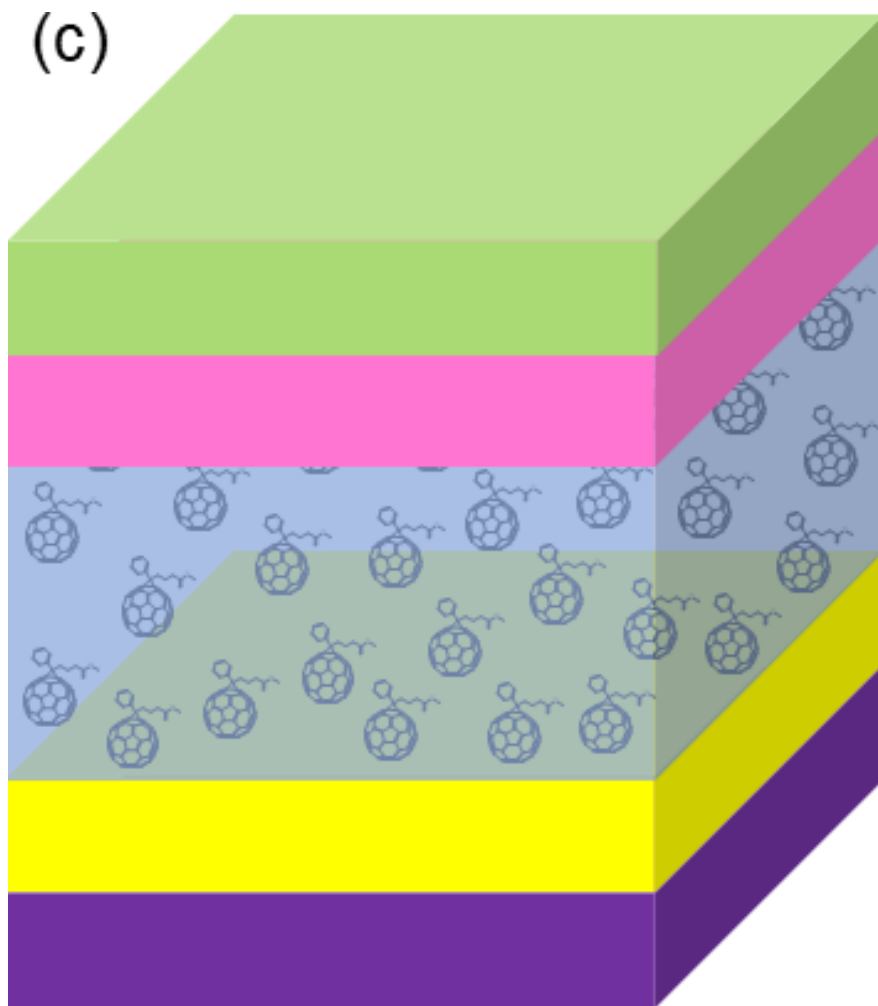
Next, the RF model was further employed to predict the best combination of nanopatterning depth and wt% of PCBM for J_{sc} , V_{oc} , ff and ECE of PCBM-PSCs with nanopatterned TiO_2 as shown in **Figure 3** . The model was trained using the J_{sc} , V_{oc} , ff , ECE, nanopatterning depths and wt% of PCBM data of PSCs with nanopatterned TiO_2 layer and PCBM-PSCs, that were obtained from previous experiments. The results demonstrated that the highest predicted ECE of 16.73% was achieved with a combination of 127 nm nanopatterning depth and 0.1 wt% of PCBM. The top ten predicted results are also tabulated in **Table 1** . Based on these findings, the best combination of nanopatterning depth and wt% of PCBM were used as a reference to fabricate PCBM-PSCs with nanopatterned TiO_2 layer.

Table 1 . Top 10 prediction for the PCBM-PSCs with nanopatterned TiO_2 layer by using ML.

Nanopatterning depth [nm]	wt% of PCBM [wt%]	J_{sc} [mA/cm ²]	V_{oc} [V]	ff	ECE [%]
127	0.10	23.16	0.95	0.75	16.73
127	0.12	23.16	0.95	0.75	16.58
132	0.10	22.73	0.94	0.74	16.27
137	0.10	22.53	0.94	0.75	16.27
142	0.10	22.53	0.94	0.75	16.26
147	0.10	22.60	0.94	0.75	16.25
152	0.10	22.19	0.94	0.75	16.23
157	0.10	22.21	0.94	0.74	16.23
127	0.07	22.83	0.95	0.75	16.22
132	0.12	22.73	0.94	0.74	16.12







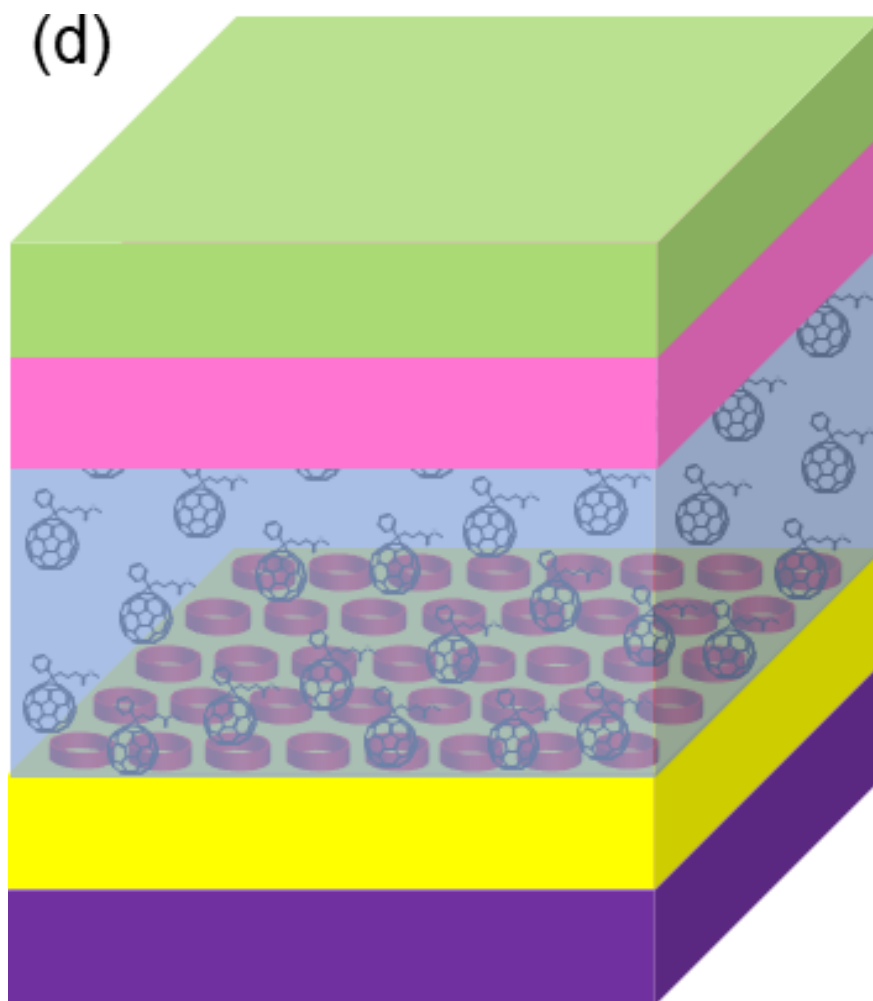


Figure 4. The solar cell structure of a) pristine PSCs, b) PSCs with nanopatterned TiO_2 layer, c) PCBM-PSCs and d) PCBM-PSCs with nanopatterned TiO_2 layer.

To have a better understanding regarding the dual effects of nanopatterning depth and wt% of PCBM on PSCs and the differences between each PSC, four types of PSCs were fabricated, as shown in **Figure 4**. The fabricated PSCs were pristine PSCs, PSCs with nanopatterned TiO_2 layer, PCBM-PSCs, and PCBM-PSCs with nanopatterned TiO_2 layer. The best combination of nanopatterning depth (127 nm) and wt% of PCBM (0.10 wt%) that yielded the highest predicted ECE was selected as a reference to fabricate the PSCs.

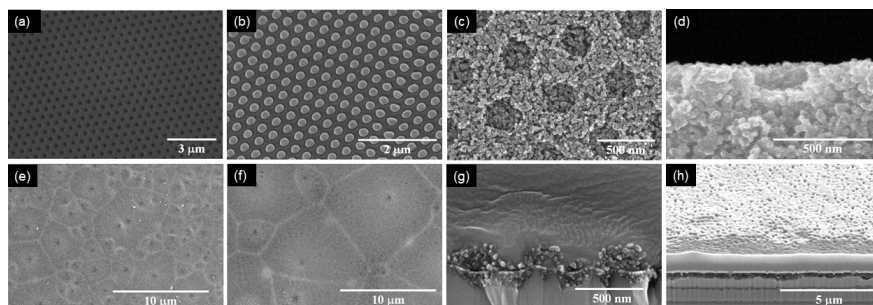


Figure 5. FE-SEM images of a) Si master, b) tilted view of PFPE mold, c) top view of nanopatterned TiO₂ layer, d) side view of nanopatterned TiO₂ layer, e) perovskite layer, and f) PCBM-perovskite layer, g) cross-sectional images of PCBM-PSCs with nanopatterned TiO₂ layer, and h) FIB image of PCBM-PSCs with nanopatterned TiO₂ layer.

Figure 5 a shows the field emission scanning electron microscopy (FE-SEM) image of the nanopatterned Si master with 250 nm pore sizes and 250 nm interpore distances. For duplication of nanopatterning on the Si master, the PFPE resin was coated on the surface of Si master and polymerized by UV irradiation for hardening, as shown in Figure 5b. A polyethylene terephthalate (PET) film was used as a flexible substrate of PFPE resin. Figure 5c visualized the form of the nanopatterned TiO₂ with a 280 nm pore size, which look like the moth-eye nanostructure. The depth of the nanopatterned TiO₂ layer is 127 nm, as shown in Figure 5d, which is the most optimized nanopatterning depth.^[14] Figure 5e and 5f show the grain boundaries of perovskite and PCBM-perovskite layers. Without PCBM, the perovskite layer has lots of grain boundaries with smaller grain sizes. However, with the incorporation of 0.10 wt% of PCBM, larger grain sizes were formed as PCBM filled the pinholes between the small grain sizes. As a result, the grain of perovskite with PCBM has larger sizes and higher density, that indicates better surface morphology of PCBM-perovskite layer.^[19] The cross-sectional image of PCBM-perovskite layer on the PCBM-PSCs with nanopatterned TiO₂ layer can be observed from Figure 5g. From the FE-SEM images, the PCBM cannot be confirmed because the resolution of FE-SEM was out of range. Thus, Fourier transform infrared (FTIR) analysis was used to verify the PCBM, which will be discussed in a later paragraph. The thicknesses of nanopatterned TiO₂ layer, perovskite, Spiro-OMeTAD, and Au are 131 nm, 400 nm, 250 nm, and 290 nm, respectively, as shown in Figure 5h.

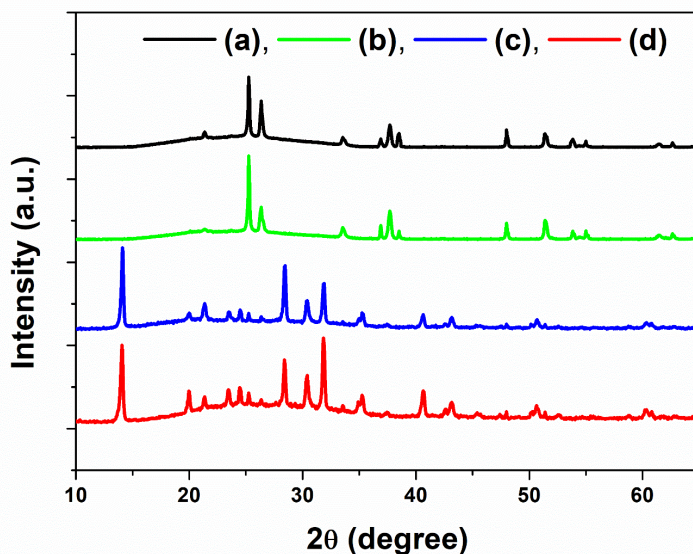


Figure 6. XRD images of a) TiO₂, b) nanopatterned TiO₂ layer, c) perovskite, and d) PCBM-perovskite layer.

X-ray diffraction (XRD) patterns in **Figure 6** confirmed the crystallinity of nanopatterned TiO₂ layer and PCBM-perovskite layer. The nanopatterned TiO₂ shows anatase phase at 2θ values of 25.2@, 37@, 38@, 38.5@, 48@, 54@, 55@, and 63@, corresponding to the (101), (103), (004), (112), (200), (105), (211), and (118) peaks.^[14, 24] For the PCBM-perovskite layer, the XRD patterns show that the presence of PCBM did not change the cell dimensions of the perovskite. Both pure perovskite and PCBM-perovskite layers exhibited diffraction peaks at 2θ values of 14.15@, 20.05@, 23.5@, 24.6@, 28.47@, 31.94@, 35.3@, 40.66@,

and 43.12°, corresponding to the (110), (112), (211), (202), (220), (310), (312), (224), and (314) crystal planes of tetragonal perovskite, respectively.^[25] The results verified that the crystalline PCBM-perovskite was well formed on the nanopatterned TiO₂ layer, thus it could achieve better ECE.

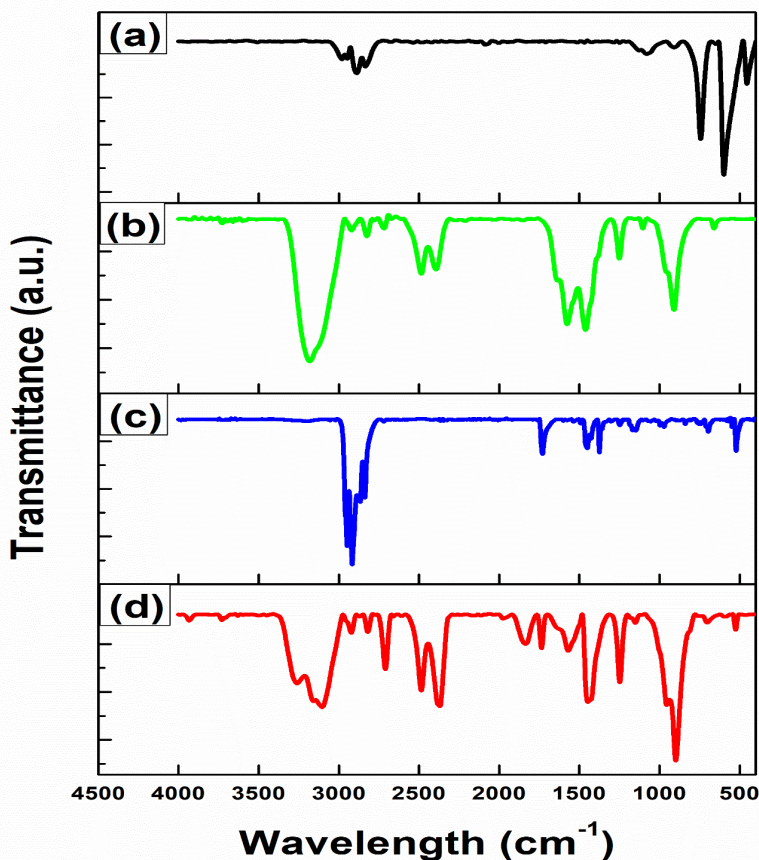


Figure 7. FTIR of a) FTO, b) perovskite/FTO, c) PCBM/FTO, and d) PCBM-perovskite/FTO.

To elaborate on the information of the PCBM-perovskite layer, FTIR spectroscopy was carried out and the results are as shown as in **Figure 7**. Figure 7 shows the comparison between the FT-IR spectra of a) FTO, b) perovskite/FTO, c) PCBM/FTO, and d) PCBM-perovskite/FTO. The peaks at 3200 and 3100 cm⁻¹ are due to the N-H stretching vibration for primary amines, and the 1600 and 1475 cm⁻¹ double bands belong to the C=C group. The C-N stretching absorption that occurs in the region from 1250-1000 cm⁻¹ indicates the aliphatic amines^[26] while the single band at 900 cm⁻¹ is corresponding to the metal iodide stretching vibration,^[27] as shown in Figure 7b.

Apart from that, the incorporation of PCBM in the PCBM-perovskite layer was confirmed by comparing Figure 7c and 7d. The absorption bands for PCBM can be observed near 3000 cm⁻¹, which indicates the sp³ C-H absorption of alkanes group while the absorption bands for C=O and C-O that appear within the range of 1750-1735 and 1300-1000 cm⁻¹ indicate that the compound is an ester. The peak at 1465 cm⁻¹ is due to the CH₂ bending absorption, which is the characteristic of methylene group^[26] and the peak at 524 cm⁻¹ belongs to C₆₀.^[28] It can be seen that the main characteristic peaks of perovskite and PCBM can be identified in Figure 7d, which indicate the good formation of the PCBM-perovskite layer.

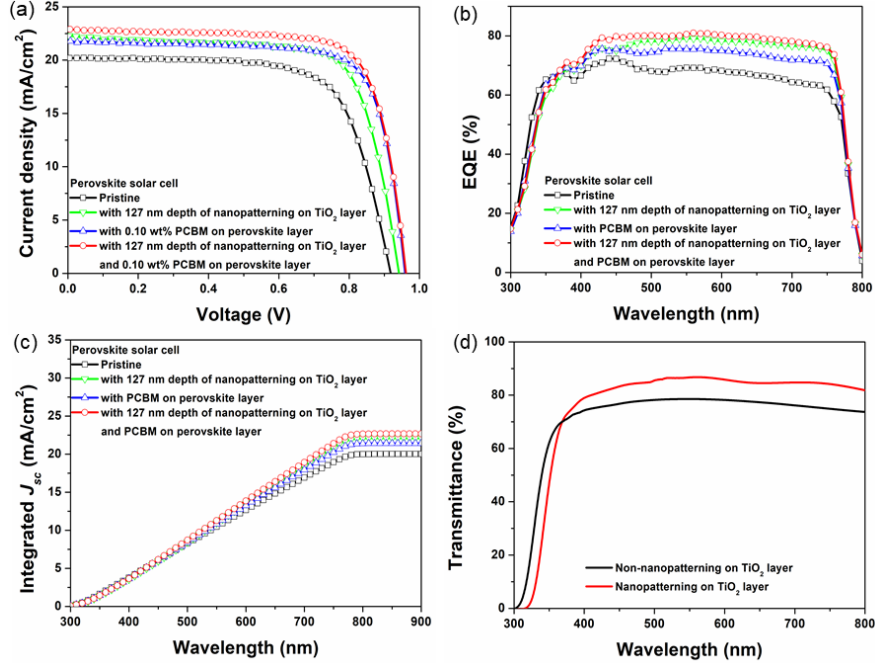


Figure 8. a) J-V curves, b) EQE, c) integrated J_{sc} , d) transmittance of PSCs. The black, green, blue, and red lines represent the pristine PSC, PSC with nanopatterned TiO_2 layer, PCBM-PSC and PCBM-PSC with nanopatterned TiO_2 layer.

Table 2 . Photovoltaic properties of the PSCs devices.

	Perovskite solar cell	J_{sc} [mA/cm ²]	V_{oc} [V]	ff	ECE [%]
(a)	Pristine	20.203	0.920	0.704	13.085
(b)	PSCs with nanopatterned TiO_2 layer	22.302	0.942	0.730	15.336
(c)	PCBM-PSCs	21.865	0.961	0.783	16.453
(d)	PCBM-PSCs with nanopatterned TiO_2 layer	22.877	0.963	0.787	17.338

The pristine PSC, PSC with nanopatterned TiO_2 layer, PCBM-PSC and PCBM-PSC with nanopatterned TiO_2 layer were fabricated and characterized by J-V curves, external quantum efficiency (EQE), integrated J_{sc} and transmittance measurement. The J_{sc} , V_{oc} , ff , and ECE of J-V curves were summarized in **Table 2**. From the results obtained, the PSCs with nanopatterned TiO_2 layer and PCBM-PSCs with nanopatterned TiO_2 layer had better J_{sc} compared to the pristine PSCs and PCBM-PSCs, as shown in **Figure 8 a**, due to the improved electron generation through light harvesting on nanopatterned TiO_2 layer.

As visualized in Figure 8b, the intensity of the pristine PSC is higher than other PSCs at the wavelengths below 350 nm. However, at wavelengths ranging from 350 nm to 800 nm, the intensity of the PCBM-PSC with nanopatterned TiO_2 layer is the highest, indicating that more electrons were generated in the range of

350 nm to 800 nm.^[14] Higher electron generation leads to a higher electron density, which increases the J_{sc} , V_{oc} and ff . Thus, the ECE of PSC will also increase. The integrated J_{sc} in Figure 8c can be calculated from Equation (1), in which F represents the Faraday constant, $E_{e\lambda}$ is the solar spectral irradiance, and N_A is the Avogadro constant. The integrated J_{sc} matched with the measured J_{sc} of all four types of PSCs.

$$J_{sc, int} = \frac{F \times \int (E_e \times EQE) d}{N_A} (1)$$

The transmittance of pristine PSCs and PCBM-PSCs with nanopatterned TiO_2 layer were measured by using UV-Vis spectrometer, as shown as in Figure 8d. Around 300 nm to 370 nm wavelengths, the transmittance of pristine PSC was higher than PCBM-PSC with nanopatterned TiO_2 layer. On the contrary, for wavelengths higher than 370 nm, the transmittance of PCBM-PSC with nanopatterned TiO_2 layer was higher than the pristine PSC. The transmittance enhancement was due to the rougher surface of PCBM-PSC with nanopatterned TiO_2 layer compared to the pristine PSC, which might induces the changes in the refractive index.^[14] Furthermore, if the angle of reflected-diffracted light is larger than the critical angle, it causes the total internal reflection because of the decrement in the refractive index values from the TiO_2 to the air.^[29] Thus, the lower the refractive index, the higher the transmittance.^[30]

On top of that, the incorporation of PCBM into perovskite also contributed to V_{oc} enhancement. This is because V_{oc} is determined by the difference between the conduction band (CB) of electron transport material (ETM) and the valence band (VB) of perovskite, as shown in **Figure 9**. Without PCBM, pristine PSCs and PSCs with nanopatterned TiO_2 layer have only one ETM, that is TiO_2 . However, with the incorporation of PCBM into perovskite, the PCBM-PSCs, and PCBM-PSCs with nanopatterned TiO_2 layer have two ETMs, that are TiO_2 and PCBM. Therefore, the CB of ETM will not depend only on the TiO_2 , but the average value between TiO_2 and PCBM. In simpler words, it can be said that the CB of ETM were elevated by PCBM, which improved V_{oc} . As the difference between the CB of ETM and the VB of perovskite in PCBM-PSCs and PCBM-PSCs with nanopatterned TiO_2 layer are higher than the pristine PSCs and PSCs with nanopatterned TiO_2 layer, therefore the V_{oc} of PCBM-PSCs and PCBM-PSCs with nanopatterned TiO_2 layer are higher.

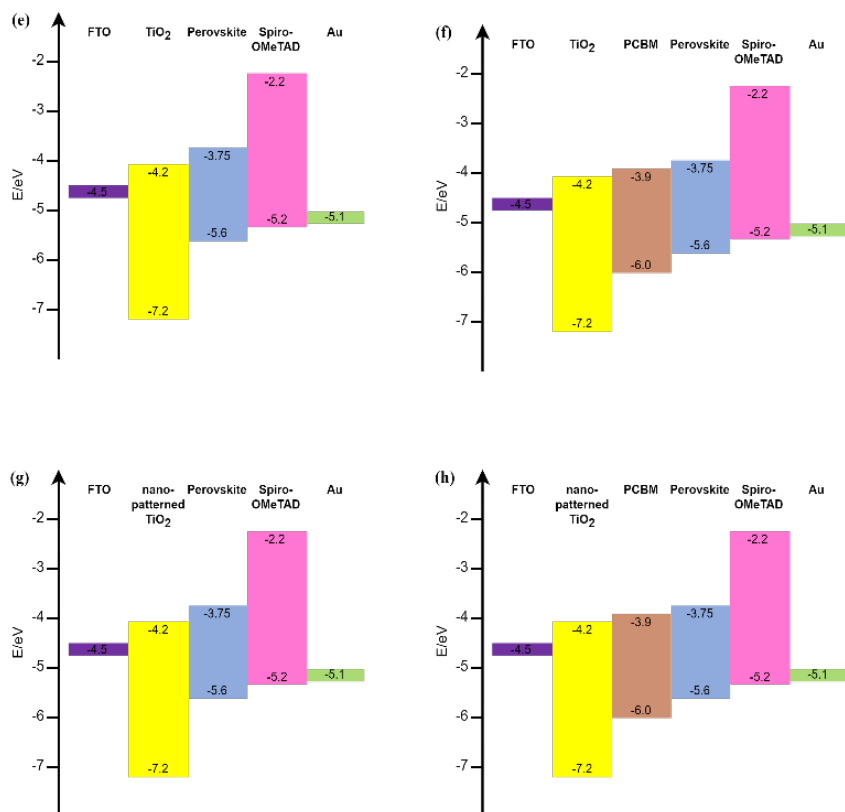


Figure 9. Energy band diagram of a) pristine PSCs, b) PSCs with nanopatterned TiO₂ layer, c) PCBM-PSCs, and d) PCBM-PSCs with nanopatterned TiO₂ layer.

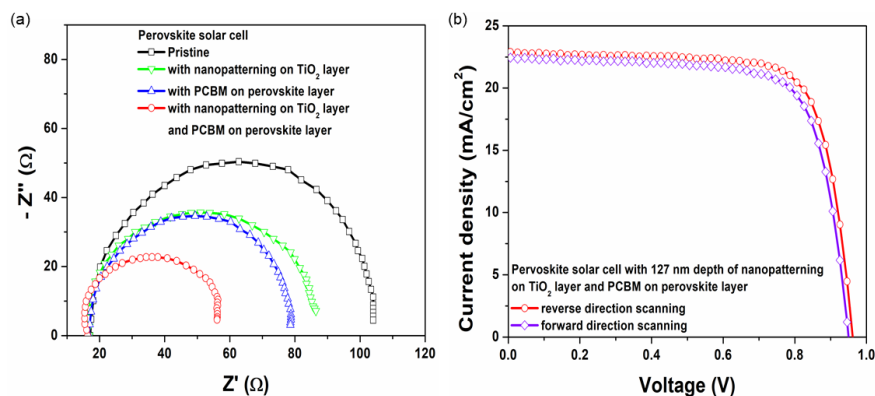


Figure 10. a) impedance of PSCs. The black, green, blue, and red lines represent the pristine PSC, PSC with nanopatterned TiO₂ layer, PCBM-PSC, and PCBM-PSC with nanopatterned TiO₂ layer. b) hysteresis graphs of PCBM-PSC with nanopatterned TiO₂ layer for forward and reverse scanning directions.

Next, to further understand the charge transport process in the pristine PSC, PSC with nanopatterned TiO₂ layer, PCBM-PSC, and PCBM-PSC with nanopatterned TiO₂ layer, electrochemical impedance spectroscopy (EIS) characterization was carried out and the results are shown in **Figure 10** a and tabulated in **Table 3**

. The series resistance (R_s) can be estimated from the high-frequency intercept on the real axis while the recombination resistance (R_{rec}) can be assigned to the recombination at the perovskite/ TiO_2 interface.^[31] By analyzing the Nyquist plots, it can be observed that the pristine PSC exhibits the largest semicircle, followed by the PSC with nanopatterned TiO_2 layer, PCBM-PSC, and PCBM-PSC with nanopatterned TiO_2 layer. The largest semicircle indicates low electron-hole density move across the perovskite interface^[32], indicating that more charge would take part in the interfacial recombination process.^[33] Therefore, as the PCBM-PSC with nanopatterned TiO_2 layer has the smallest semicircle, the results further validate that the nanopatterning and PCBM were able to suppress the recombination and increase the electron transport property, owing to the increment in the electron density and the improved surface morphology of PCBM-perovskite layer.

Aside from that, for reverse scanning from positive to negative voltage, the efficiency was 17.336%. When the direction was changed to forward scanning, the efficiency reduced to 16.256%, which is only a 6.23% decrement, indicating that the PCBM-PSC with nanopatterned TiO_2 layer has only a small and negligible hysteresis as represented in Figure 10b and **Table 4**. These results further showed that PCBM plays a significant role in the suppression of hysteresis. Previous studies have proposed that the origin of hysteresis in PSCs is due to the ion migration and vacancies on perovskite layer. Therefore, through the diffusion of PCBM into the grain boundaries in perovskite, the hysteresis can be suppressed through the formation of physical hindrance for the ion migration or occupying some vacancy space in the perovskite.^[34]

Table 3. EIS parameters for the PSCs.

	Perovskite solar cell	R_s [Ω]	R_1 [Ω]	R_2 [Ω]
(a)	pristine	14.73	43.16	50.76
(b)	with 127 nm nanopatterned TiO_2 layer	14.64	33.61	41.25
(c)	with 0.10 wt% PCBM on perovskite layer	14.71	29.83	37.34
(d)	with 127 nm nanopatterned TiO_2 layer and 0.10 wt% PCBM on perovskite layer	13.68	21.02	25.14

Table 4 . Hysteresis of PCBM-PSCs with nanopatterned TiO_2 layer.

	PCBM-PSCs with nanopatterned TiO_2 layer	J_{sc} [mA/cm^2]	V_{oc} [V]	ff	η [%]
(a)	reverse direction scanning	22.877	0.963	0.787	17.338
(b)	forward direction scanning	22.492	0.951	0.760	16.256

3. Conclusion

In conclusion, ML has been successfully implemented in this research to integrate different factors and predict the best combination of nanopatterning depth and wt% of PCBM. The best combination predicted were at 127 nm nanopatterning depth and 0.10 wt% of PCBM with J_{sc} , V_{oc} , ff and ECE values of 23.162 mA/cm², 0.953 V, 0.753 and 16.727%. As the predicted performance of PCBM-PSCs with nanopatterned TiO₂ layer were higher than the PSCs with nanopatterned TiO₂ layer and PCBM-PSCs, the results proved that ML were capable to learn the relationship between two different factors and predict the performance of new PSCs. Therefore, with the assistance of ML, PCBM-PSCs with nanopatterned TiO₂ layer were fabricated and characterized. The consistencies of experimental results with the predicted values further validate the reliability of the ML model. Through this approach, it has been observed that nanopatterning depth significantly increased the J_{sc} , attributed to the improved light harvesting through nanopatterning. The nanopatterned TiO₂ layer was able to enhance electron generation, which leads to a higher electron density and thus increases the J_{sc} . Furthermore, the incorporation of PCBM into the perovskite layer enhanced the electron transport property of PSCs, yielding to the increment in V_{oc} and ff . This is because PCBM were able to fill in the pinholes and grain boundaries between the perovskites, resulting in a formation of larger perovskite-PCBM grain sizes. Experimentally, the highest ECE obtained was 17.336%, which represented a 32.5% improvement compared to the pristine PSC. These results pave the way to understand the dual effects of nanopatterning depth and wt% of PCBM in the performance of PCBM-PSCs with nanopatterned TiO₂ layer and represent a significant step towards the development of PSCs more efficiently by examining and uncovering patterns of the available data through ML.

4. Experimental Section/Methods

4.1. Machine Learning

4.1.1. Prediction of the most optimal nanopatterning depth and wt% of PCBM in PCBM-PSCs with nanopatterned TiO₂ layer

The objective to predict J_{sc} , V_{oc} , ff and ECE of PCBM-PSCs with nanopatterned TiO₂ layer was formulated as a regression problem and 108 datasets were used to train the ML model and another 12 datasets were used for validation. The data consists of J_{sc} , V_{oc} , ff and ECE for the PSCs with nanopatterned TiO₂ layer and PCBM-PSCs that were collected through previous experiments. In this study, a Random Forest regression model was used to train the datasets. Then, the multioutput regressor, which fits one regressor per target, was opted to predict the J_{sc} , V_{oc} , ff and ECE, and Optuna was used for hyperparameter tuning and obtaining the most optimal hyperparameter for the model, as shown in the **Table 5** below.

Table 5 . Optimal parameters for the ML model

Hyperparameter	Optimal value
n_estimators	86
max_depth	4
max_features	sqrt
random_state	98
min_samples_split	0.0087

4.2. Device Fabrication

4.2.1. Preparation of perfluoropolyether (PFPE) mold

The PFPE resin (Fluorolink MD700, Solvay Solexis, Milan, Italy) was mixed with 3% w/w photoinitiator (Darocur 1173, Sigma Aldrich, St. Louis, MO, USA) to create the UV-curable resin. Then, the patterned silicon substrate (e.g., Si master) was coated with the UV-curable resin and covered with polyethylene terephthalate (PET) film as a backplane. The PET film was then rolled over to the UV-curable resin to

distribute it evenly and the mixture was cross-linked by exposure to UV light at 365 nm for 5 minutes. After the curing process, the PFPE mold was detached from the Si master.

4.2.2. Preparation of perovskite precursor solution

Methylammonium iodide (MAI) was prepared by mixing 25 mL of methylamine (33 wt% in ethanol, Sigma Aldrich, St. Louis, MO, USA) and 10 ml of hydroiodic acid (55–58%, Kanto Chemical, Tokyo, Japan) in a round-bottom flask, which was kept in an ice bath for 2 hours. The resulting product was then obtained using a rotary evaporator at 60°C for 1 hour. After evaporating, the precipitates were recrystallized several times using ethanol (99.9%, Daejung Chemicals, Siheung-si, Korea) and diethyl ether (99%, Daejung Chemicals, Siheung-si, Korea), followed by an overnight drying at 60°C in a vacuum oven. Finally, 45 wt% of MAI and lead (II) iodide with a 3:1 molar ratio were stirred in N,N-dimethylformamide (DMF, 99.8%, Sigma Aldrich, St. Louis, MO, USA) at 90 °C for 1 hour.

4.2.3. Preparation of PCBM-perovskite precursor solution

The perovskite solution was created by mixing MAI and lead (II) iodide in a 3:1 molar ratio, 45 wt% with DMF. The perovskite-PCBM layer was prepared by dissolving PCBM (99.5%, Nano-C) into chlorobenzene, then mixing the solution with the perovskite precursor solution.

4.2.4. Preparation of hole transport materials (HTM) solution

To prepare the hole transport materials, 73.5 mg of spiro-OMeTAD (99.62%, Feiming Chemical Limited, Shenzhen, China), 17 μ l of bis(trifluoromethane)sulfonamide lithium salt (Li-TFSI, 99.95%, Sigma Aldrich, St. Louis, MO, USA) solution (574.2 mg of Li-TFSI in 1 ml of acetonitrile), and 36.2 μ l of 4-tert-butylpyridine (98%, Sigma Aldrich, St. Louis, MO, USA) were stirred at room temperature for 2 hours in 1 ml of chlorobenzene (99.8%, Sigma Aldrich, St. Louis, MO, USA).

4.2.5. Fabrication of PCBM-PSCs with nanopatterned TiO_2 layer

The fluorine-doped tin oxide (FTO) glass was cleaned using water, ethanol, and acetone. Then, the compact TiO_2 layer was created by spin-coating a precursor solution made of 1 ml of titanium diisopropoxide bis(acetylacetonate) (75 wt% in isopropanol, Sigma Aldrich, St. Louis, MO, USA) in 6 ml of butanol (99%, Daejung Chemicals, Siheung-si, Korea) onto the FTO at 4000 rpm for 20 s, followed by annealing at 250°C for 10 min. This process was repeated twice. To form the mp- TiO_2 layer, 1 g of TiO_2 paste (Ti-Nanoxide T/SP, Solaronix, Aubonne, Switzerland) was diluted in 12 ml of anhydrous ethanol (99.9%, Daejung Chemicals, Siheung-si, Korea), and spin-coated on a compact TiO_2 /FTO. After slightly evaporating the solvent by prebaking on a hotplate at 70°C for 1 min, the PFPE mold was placed on the mp- TiO_2 /compact TiO_2 /FTO substrate and heat-pressed for 5 min at 70°C with a pressure of 2 bar. After removing the mold, the resulting nanopatterned mp- TiO_2 /compact TiO_2 /FTO substrate was then annealed at 500 °C for 1 hour. The PCBM-perovskite layer was created by spin coating the PCBM-perovskite precursor solution at 700 rpm onto the nanopatterned mp- TiO_2 layer through the hot-casting technique at 90 °C, followed by annealing at 130 °C for 1 hour. The HTM layer was spin coated at 4000 rpm for 60 s and dried overnight in a glovebox. All the procedure were conducted inside a dried air-filled glovebox. Finally, the Au electrode was deposited through thermal evaporation.

4.3. Analysis

A field emission scanning electron microscope (FE-SEM, SU-70, Hitachi) was used to examine the morphology and thickness of the device configurations while an X-ray diffractometer (Rigaku Corp., D/max-2500, Tokyo, Japan) was used to confirm the crystallinity of TiO_2 and perovskite layers. To measure the transmittance, a UV-Vis spectrophotometer (Jasco International Co., Ltd., V-730, Tokyo, Japan) was used and the infrared spectra were recorded on the Fourier-transform infrared (FTIR) spectrometer (Nicolet 6700, Thermo Scientific) in the range of 600 – 4000 cm^{-1} . Then, a solar simulator (Newport Corp., Model 94022A, Irvine CA, USA) with a source meter (Keithley Instruments Inc., Keithley 2400, Cleveland, OH, USA)

under AM 1.5 illumination (100 mW/cm²) was used to characterize the photovoltaic properties of PSCs. The characterization was carried out at the Future Energy Convergence Core Center (FECC). All devices were measured by masking 0.1256 cm² of the active area with a mask under argon condition. The solar cell quantum efficiency measurement system (PV Measurements Inc., QEX7, Point Roberts, WA, USA) was also used to measure the incident photon to electron conversion efficiencies. Electrochemical impedance spectroscopy was performed using a potentiostat (Solartron 1287) and frequency response analyzer (Solartron 1260) in the range of 10⁻² and 10⁶ Hz. The measurements were analyzed using the ZView software (Solartron Analytical) with the aid of appropriate equivalent circuit, where the applied bias voltage and the amplitude of alternating current was set at the open circuit voltage (V_{oc}). The impedance measurements were carried out at open-circuit potential under AM 1.5 illumination.

Conflicts of Interest

The authors declare no conflict of interest.

Supporting Information

Supporting Information is available from the Wiley Online Library or from the author.

Acknowledgements

This research was supported by the “Human Resources Program in Energy Technology” of the Korea Institute of Energy Technology Evaluation and Planning (KETEP), which received financial resources from the Ministry of Trade, Industry & Energy, Republic of Korea (No. 20204010600470), by the Korea Evaluation Institute of Industrial Technology (KEIT) and the Ministry of Trade, Industry & Energy (MOTIE) of the Republic of Korea (No. 20018608), and by Basic Science Research Program through the National Research Foundation of Korea (NRF) funded by the Ministry of Education (No. 2022R1I1A1A01064236).

Received: (will be filled in by the editorial staff) Revised: (will be filled in by the editorial staff) Published online: (will be filled in by the editorial staff)

References

- [1] M. I. Jordan, T. M. Mitchell, *Science* **2015** , 349, 255.
- [2] W. Liu, Y. Lu, D. Wei, X. Huo, X. Huang, Y. Li, J. Meng, S. Zhao, B. Qiao, Z. Liang, Z. Xu, D. Song, *Journal of Materials Chemistry A* **2022** , 10, 17782.
- [3] Y. Liu, W. Yan, S. Han, H. Zhu, Y. Tu, L. Guan, X. Tan, *Solar RRL* **2022** , 6.
- [4] A. Marchioro, J. Teuscher, D. Friedrich, M. Kunst, R. van de Krol, T. Moehl, M. Grätzel, J.-E. Moser, *Nature Photonics* **2014** , 8, 250.
- [5] C. Barugkin, J. Cong, T. Duong, S. Rahman, H. T. Nguyen, D. Macdonald, T. P. White, K. R. Catchpole, *J Phys Chem Lett* **2015** , 6, 767.
- [6] C. Ma, Y. Shi, W. Hu, M. H. Chiu, Z. Liu, A. Bera, F. Li, H. Wang, L. J. Li, T. Wu, *Adv Mater* **2016** , 28, 3683.
- [7] Q. Zhang, D. Myers, J. Lan, S. A. Jenekhe, G. Cao, *Phys Chem Chem Phys* **2012** , 14, 14982.
- [8] M. R. Luo, *Encyclopedia of Color Science and Technology* , Springer, New York, USA **2016** .
- [9] S. M. Kang, S. Jang, J. K. Lee, J. Yoon, D. E. Yoo, J. W. Lee, M. Choi, N. G. Park, *Small* **2016** , 12, 2443.
- [10] M. T. Hörantner, W. Zhang, M. Saliba, K. Wojciechowski, H. J. Snaith, *Energy & Environmental Science* **2015** , 8, 2041.
- [11] K. Yamamoto, T. Kuwabara, K. Takahashi, T. Taima, *Japanese Journal of Applied Physics* **2015** , 54.

- [12] J. Wei, R.-P. Xu, Y.-Q. Li, C. Li, J.-D. Chen, X.-D. Zhao, Z.-Z. Xie, C.-S. Lee, W.-J. Zhang, J.-X. Tang, *Advanced Energy Materials* **2017** , 7.
- [13] D. L. Wang, H. J. Cui, G. J. Hou, Z. G. Zhu, Q. B. Yan, G. Su, *Sci Rep* **2016** , 6, 18922.
- [14] H. Y. Yang, A. Chuquer, S. H. Han, G. S. Gaudel, X. H. Pham, H. M. Kim, W. J. Yun, B. H. Jun, W. Y. Rho, *Int J Mol Sci* **2021** , 22.
- [15] J. Hu, X. Xiong, W. Guan, H. Long, *Materials Today Energy* **2021** , 21.
- [16] T. Gatti, E. Menna, M. Meneghetti, M. Maggini, A. Petrozza, F. Lamberti, *Nano Energy* **2017** , 41, 84.
- [17] N. Martín, *Advanced Energy Materials* **2017** , 7.
- [18] A. Abrusci, S. D. Stranks, P. Docampo, H. L. Yip, A. K. Jen, H. J. Snaith, *Nano Lett* **2013** , 13, 3124.
- [19] C.-H. Chiang, C.-G. Wu, *Nature Photonics* **2016** , 10, 196.
- [20] L. Breiman, J. Friedman, R. Olshen, C. Stone, *Group* **1984** , 37, 237.
- [21] S. Wright, *Journal of Agricultural Research* **1921** , 10, 557.
- [22] C. Sammut, G. I. Webb, *Encyclopedia of Machine Learning* **2010** , 653.
- [23] D. Chicco, M. J. Warrens, G. Jurman, *PeerJ Comput Sci* **2021** , 7, e623.
- [24] K. Thamaphat, P. Limsuwan, B. Ngotawornchai, *Kasetsart J. Nat. Sci.* **2008** , 42, 357.
- [25] Y. Zhao, K. Zhu, *The Journal of Physical Chemistry Letters* **2013** , 4, 2880.
- [26] D. L. Pavia, G. M. Lampman, G. S. Kriz, J. A. Vyvyan, *Introduction to Spectroscopy*, Cengage Learning, Boston **2013** .
- [27] Y. Kesari, A. Athawale, *Materials Letters* **2015** , 159, 87.
- [28] W. Kratschmer, Lowell D. Lamb, K. Fostiropoulos, Donald R. Huffman, *Nature* **1990** , 347.
- [29] K. P. Kim, W. H. Kim, S. M. Kwon, J. Y. Kim, Y. S. Do, S. Woo, *Nanomaterials (Basel)* **2021** , 11.
- [30] W. K. Kuo, J. J. Hsu, C. K. Nien, H. H. Yu, *ACS Appl Mater Interfaces* **2016** , 8, 32021.
- [31] K. Wang, Y. Shi, B. Li, L. Zhao, W. Wang, X. Wang, X. Bai, S. Wang, C. Hao, T. Ma, *Adv Mater* **2016** , 28, 1891.
- [32] S. M. Abdulrahim, Z. Ahmad, M. Q. Mehmood, S. Paek, J. Bhadra, N. J. Al-Thani, M. K. Nazeeruddin, A. Belaidi, M. Amani, *Journal of Electroanalytical Chemistry* **2021** , 902.
- [33] D. Li, C. Sun, H. Li, H. Shi, X. Shai, Q. Sun, J. Han, Y. Shen, H. L. Yip, F. Huang, M. Wang, *Chem Sci* **2017** , 8, 4587.
- [34] Y. Zhong, M. Hufnagel, M. Thelakkat, C. Li, S. Huettner, *Advanced Functional Materials* **2020** , 30.